Supplementary Materials for

Vibrationally Promoted Dissociation of Water on Ni(111)

P. Morten Hundt, Bin Jiang, Maarten E. van Reijzen, Hua Guo,* Rainer D. Beck*

*Corresponding author. E-mail: hguo@unm.edu (H.G.); rainer.beck@epfl.ch (R.D.B.)

This PDF file includes:

Materials and Methods
Figs. S1 to S8
Tables S1 to S6
References (*47–83*)

Materials and Methods

S-I. Experiment
S-Ia. Experimental details
       The experiments were conducted using a three-fold differentially pumped continuous molecular beam source coupled to an ultra-high vacuum (UHV) surface science chamber (*28*). A molecular beam of D_2O was generated by bubbling pure helium (99.9999%) with a backing pressure of 5 bar through a reservoir containing pure D_2O (99.9%) and expanding the gas mixture through a temperature controlled nozzle of 50 μm diameter into the vacuum of the first differential pumping stage where a molecular beam was isolated from the expansion using a 1 mm diameter nickel skimmer (*29*). The D_2O was carefully degassed with at least ten freeze-pump-thaw cycles in order to eliminate contaminations such as O_2 and CO_2.

       The molecular beam speed was controlled using different nozzle temperatures in the range of 373 K to 773 K which resulted in translational energies of 36.5 kJ/mol to 74 kJ/mol with an energy spread of *ΔE/E*=0.16 to 0.29 determined by measuring the time-of-flight of the molecules with a mass-spectrometer in combination with a fast chopper wheel. The D_2O molecules impinged on a Ni(111) surface at normal incidence that was cleaned by argon ion sputtering (1000 eV (1 eV=96.485 kJ/mol) kinetic energy) and annealed to 1000 K before the experiment. The surface temperature during the molecular beam deposition and Auger analysis was 300 K. The cleanliness of the surface was verified before every deposition experiment using Auger electron spectroscopy (AES). The miscut of the Ni(111) surface is smaller than 0.1°.

S-Ib. Quantum-state preparation
       Quantum-state specific preparation by rapid adiabatic passage (*27*) of the incident D_2O reactant molecules was achieved by infrared pumping using the continuous infrared idler output of two optical parametric oscillators (OPOs) with high output power (>1W) and a tuning range from 2500 cm^{-1} to 3100 cm^{-1}. The OPO idler outputs were maintained resonant with the selected D_2O transitions in the molecular beam by active stabilization to the same rovibrational transitions detected as Doppler free absorptions in two static gas cells. OPO-1, used for v_3 =1←0 excitation of the v_3 antisymmetric OD-stretch mode, was stabilized to a Lamb dip(*47*) of the R_{11}(1)-v_3 transition at 2808.76 cm^{-1}. The Lamb dip was detected by retroreflection of 5% of the OPO-1 idler power through a static gas cell filled with.100 μbar of D_2O vapor. With OPO-1 locked to the Lamb dip, another 25% of the output power were used to pump the D_2O v_3=1←0 transition in a second static gas cell to create a Doppler free absorption signal for the v_3=2←1 that was used to lock OPO-2 to a v_3=2←1, R_{12}(2) transition. Using this technique both OPOs could be stabilized to two connected infrared transitions for double resonance excitation to better than 3 MHz within the homogeneous line widths for the molecular beam.

       A pyroelectric detector, which would be inserted into the molecular beam, was used to quantify the flux of vibrationally excited D_2O molecules obtained by infrared pumping. Figure S2 shows the detector signal obtained for single resonance (v_3) and double resonance ($2v_3$) excitation. The fact that for $2v_3$ excitation the detector signal doubles compared to v_3 excitation, shows that OPO-2 transfers the complete v_3 population, created by OPO-1, into the final state $2v_3$.

S-Ic. Reaction product detection

Dissociation of incident D_2O leaves the chemisorbed dissociation products OD(ads) + D(ads) on the Ni(111) surface. At a surface temperature of T_S=300 K neither dehydrogenation of OD(ads) nor recombinative desorption of D_2 is expected. Hydrogen desorption from a Ni(111) surface was reported by Christmann et al. (48) to start at T_S=370 K. The activation energy for the dehydrogenation of an adsorbed OD is even than for the initial dissociation of water (49). Therefore we detect OD(ads) via the AES oxygen signal near 520 eV as the dissociation product of D_2O on Ni(111). At T_S=300 K water does not adsorb molecularly on a Ni(111) surface because it desorbs already at a surface temperature of $T_d \approx 170$ K (50). Hence, any oxygen that is detected by AES after a deposition of D_2O at T_S=300 K is due to dissociation of D_2O provided there is no oxygen containing contamination in the molecular beam. Careful degasing of the D_2O by at least 10 pump-freeze-thaw cycles was performed to exclude the possibility of a O_2 or CO_2 contamination from dissolved air. We calibrated the AES signal detected on the Ni(111) surface in terms of oxygen coverage using O_2 depositions that lead to a known saturation coverage. The calibrated AES signal allowed us to quantify the amount of oxygen that was deposited locally as a spot on the surface by the incident beam of D_2O. We used a computer controlled stepper motor to move the sample surface across the AES electron beam in steps of 0.25 mm and measured the AES oxygen signal (490-530 eV) and the nickel signal (800-850 eV) for typically 40 positions across the surface. In this way we recorded O/Ni AES profiles that yield the local oxygen surface coverage in monolayers (ML) (see Figure S3). For AES data analysis, we perform a background subtraction over the whole surface to account for CO adsorption from the UHV background, followed by averaging the six highest points of the O/Ni signal on the top of the oxygen spot formed by the incident D_2O beam. The baseline subtraction was done by creating a baseline consisting of six points of which two are placed before the first spot, two between the spots and two after the second spot, and subtracting it from the data (see Figure S3). The baseline was chosen to be adjustable in order to account for the continuing uptake of CO from the UHV background during the 30 min AES analysis. Using the oxygen coverage measured by AES, the incident D_2O dose via the pressure rise in the UHV chamber by a calibrated mass spectrometer, and the excited fraction of D_2O by the pyroelectric detector, we are able to calculate the initial state resolved dissociation probability S_0 (sticking coefficient) of the incident D_2O for a coverage of typically 5-10% of a monolayer.

S-Id. S-shaped reactivity curves

The state resolved experimental data (v_3, $2v_3$) were parameterized by S-shaped reactivity curves proposed by Luntz (38):

$$S_0(E_t, v) = \frac{1}{2}\left(1 + \operatorname{erf}\left|\frac{E_t - E_0^v}{W}\right|\right). \tag{1}$$

This expression describes the state resolved reactivity S_0 as function of incident translational energy E_t assuming a Gaussian distribution of barrier heights of width W and an average barrier height of $\boldsymbol{E_0^v}$ that depends on the vibrational state v. With a constant width of W=62.4 kJ/mol, we obtain the average barrier heights of $\boldsymbol{E_0^{v3}}$=213±0.5 kJ/mol and $\boldsymbol{E_0^{2v3}}$=176±1 kJ/mol by fitting expression (1) to the state resolved reactivity data for the v_3 and $2v_3$ state respectively.

S-II. Theory
S-IIa. Electronic Structure Calculations

All plane-wave density functional theory (DFT) calculations in this work have been performed with the Vienna Ab initio Simulation Package (VASP) (32-33). In the DFT calculations, the Ni(111)

surface was modeled using a three-layer slab with a separation of 15 Å in the Z direction and the water molecule was placed above a 2×2 (1/4 ML coverage) surface unit cell. The interaction between the ionic cores and electrons was described with the projector-augmented wave (PAW) method (*51*), and the Kohn-Sham valence electronic wavefunction was expanded in a plane-wave basis set (*52*) with a cutoff at 400 eV. The Brillouin zone was sampled with a 3×3×1 Monkhorst-Pack k-points grid mesh (*53*). The generalized gradient approximation (GGA) was used to treat the electron exchange-correlation effects (*54*). In most of the following calculations, the Perdew-Wang (PW91) functional (*55*) was used, but the Perdew-Burke-Ernzerhof (PBE) (*54*) and revised PBE (RPBE) functionals (*39*) were also used for comparison. Due to the open-shell nature of the Ni atom, the spin-polarized model was used and found to provide better estimation of the reaction barrier, in accord with earlier studies. The optimized lattice constant for bulk Ni obtained in this work (3.518 Å) is in excellent agreement with the experimental value (3.524 Å) (*56*). All surface atoms were fixed at their bulk positions in most calculations, except when the lattice effects were considered. In the latter case, the top two surface layers were allowed to relax at the reaction saddle point geometry.

The aforementioned slab model is computationally efficient, which is necessary because of a large number of points needed to fit the potential energy surface (PES). In order to validate our model, stationary points associated with the O-H bond dissociation process were determined. To this end, the physisorbed H_2O, which was assigned as the initial state (IS), and the co-adsorbed OH and H, which was assigned as the final state (FS), were firstly obtained, followed by the optimization of the transition state (TS) using the climbing-image nudged elastic band (CI-NEB) method (*57-58*). The minimum energy path (MEP) was discretized by five images between IS and FS, with TS as the highest image along the MEP. The saddle point is confirmed by the presence of a single imaginary frequency. The barrier height converged well with respect to the number of layers, the number of k-points, the size of unit cell, and the kinetic energy cutoff. In addition, the adsorption and activation energies obtained from calculations with top two layers relaxed were also tested against those obtained in rigid surface calculations with all surface atoms fixed at their bulk positions.

S-IIb. Potential Energy Surface

Following our previous work on H_2O/Cu(111) (*15, 17, 20*), we employed the permutation invariant polynomial approach of Bowman and coworkers (*34*) to construct a reduced-dimensional PES for the H_2O/Ni(111) system. As shown in Fig. 1, our six-dimensional (6D) model includes the internal modes of H_2O expressed in Jacobi coordinates (r_1, r_2, and θ_1), the normal incident coordinate (Z) that is the distance between the center of mass (COM) of H_2O and the surface, and two rotational angles (θ_2 and φ) for the H_2O moiety. The degrees of freedom neglected in this model consist of translational coordinates of the H_2O moiety in the XY plane and the rotational angle of H_2O moiety around the surface normal. Although this reduced-dimensional model does not describe the product channel well (*17*), it is sufficient for our quantum dynamical calculations based on the flux method (*vide infra*).

This 6D model can be considered as a four-atom system consisting of H_2O and a *pseudo* 'surface atom' which represents the Ni(111) surface. The permutation invariant polynomial approach of Bowman and coworkers (*34*) was thus used to represent the PES:

$$V_{H_2O+Ni} = \sum_{l_1 l_2 l_3 l_4 l_5 l_6} c_{l_1 l_2 l_3 l_4 l_5 l_6} \hat{S}[y_{12}^{l_1} y_{13}^{l_2} y_{14}^{l_3} y_{23}^{l_4} y_{24}^{l_5} y_{34}^{l_6}], \tag{2}$$

where $\hat{S}$ is the symmetrization operator. H, H, O, and the 'surface atom' are labeled as 1, 2, 3, and 4, respectively, and $y_{ij}=\exp(-r_{ij}/a)$ where r_{ij} is the distance between atoms i and j, a=2.0 bohr (1 bohr = 0.5292 Å). Here, the 'surface atom' is placed at the projection of the H_2O COM in the XY plane.

Geometries of the DFT points were largely chosen near the MEP for the dissociative chemisorption of H_2O. In addition, classical trajectories were launched from the reactant asymptote to explore the reactive configuration space, and additional points were added. Each new point satisfies the selection criterion that the Euclidean distance between this point and every existing point is larger than 0.2 Å. This procedure is repeated until the PES covers all relevant configuration space, yielding the final data set of 22,085 points. In the fitting, all terms up to total degree ($l = l_1 + l_2 + l_3 + l_4 + l_5 + l_6$) of 6 were included, resulting in 502 terms. The expansion coefficients were determined by a weighted least squares method. In order to give a better description of the stationary points, points in the reactant asymptote and near the physisorption well were assigned a weight of five, while those near the transition state were assigned a weight of ten.

To avoid the unphysical anisotropy in the reactant asymptote due to the finite size of the unit cell in the periodic DFT calculations, it is desirable to switch the asymptotic region of the H_2O/Ni(111) PES to the H_2O PES in gas phase, as has been done for the CH_4/Ni(111) PES by Kroes *et al.* (*59*) and for our own H_2O/Cu(111) PES (*20*). To this end, a three-dimensional PES for the isolated H_2O system was constructed using the same approach. Specifically, 2141 points were calculated in a box with a single H_2O molecule. The PES was fit with permutation invariant polynomials up to the tenth order,

$$V_{H_2O} = \sum_{l_1 l_2 l_3} c_{l_1 l_2 l_3} \hat{S}[y_{12}^{l_1} y_{13}^{l_2} y_{23}^{l_3}], \qquad (3)$$

resulting in 161 coefficients. Again, a weighted least squares method was used to obtain the expansion coefficients, in which weights of points near the H_2O equilibrium were increased by a factor of eight. The final PES is expressed as,

$$V = SV_{H_2O} + (1-S)V_{H_2O+Ni}, \qquad (4)$$

where the switching function is defined as follows (in Å):

$$S = \left(\frac{1+\tanh\left[(r_{14}-4.2)\right]}{2}\right)\left(\frac{1+\tanh\left[(r_{24}-4.2)\right]}{2}\right)\left(\frac{1+\tanh\left[(r_{34}-4.2)\right]}{2}\right). \quad (5)$$

S-IIc. Quantum Wavepacket Theory
Our reduced-dimensional quantum dynamical model has been discussed in detail in our previous work for H_2O/Cu(111) (*15, 17, 20*), so only brief outline will be given here. This 6D Hamiltonian for the dissociative chemisorption of D_2O on Ni(111) is expressed as follows ($\hbar = 1$ hereafter):

$$\hat{H} = -\frac{1}{2\mu_1}\frac{\partial^2}{\partial r_1^2} - \frac{1}{2\mu_2}\frac{\partial^2}{\partial r_2^2} - \frac{1}{2M}\frac{\partial^2}{\partial Z^2} + \frac{\hat{j}^2}{2\mu_1 r_1^2} + \frac{(\hat{J}-\hat{j})^2}{2\mu_2 r_2^2}$$
$$+ V(r_1, r_2, Z, \theta_1, \theta_2, \varphi),$$

(6)

where the r_1 is the bond length of non-dissociative OD bond, r_2 the distance between the COM of OD and D, and Z the distance between the D$_2$O COM and surface. $\mu_1 = m_D m_O /(m_D + m_O)$, $\mu_2 = m_{OD} m_D /(m_{OD} + m_D)$, $M = m_{D_2O}$. $\hat{j}$ and $\hat{J}$ are the angular momenta for the OD fragment and D$_2$O triatom, respectively. V is the PES. The coordinates ignored in this model include the translational degrees of freedom parallel to the surface, but they are not considered essential for the reaction.

The Hamiltonian was represented with a mixed discrete variable representation (DVR) and finite basis representation (FBR) (60). The Z and r_2 coordinates were discretized with the sine DVR (61), while r_1 was treated as non-reactive with a potential optimized DVR (PODVR) (62-63). An L-shape scheme was imposed to save computational effort, in which the grids in Z were divided into an interaction region and an asymptotic region, one can use only a small number of vibrational basis functions in r_2 coordinates in the asymptotic region instead of the uniform sine DVR, thus reducing the size of basis set. We focused in this work on the vibrational effects with the D$_2$O molecule in its rotational ground state, the normalized associated Legendre functions $\bar{P}_J^K(\cos\theta_2)$ and the exponential Fourier function ($\exp(iK\varphi)$) were therefore used for describing the rotation of the triatom. The other rotational/bending degree of freedom is also described by the normalized associated Legendre functions $\bar{P}_j^K(\cos\theta_1)$. Note that our model can be readily extended to treat rotational excited states of D$_2$O, as discussed in our recent work (20). In that case, the basis for the H$_2$O overall rotational is described in terms of the Wigner functions $D_{MK}^J(\phi, \theta_2, \varphi)$,

which can be expressed as $\sqrt{\frac{2J+1}{8\pi^2}} e^{iM\phi} d_{MK}^J(\theta_2) e^{iK\varphi}$ (64). Here, M is the projection of J on the surface normal, which is conserved within the flat surface model because the potential is independent of the azimuthal angle ϕ. As a result this degree of freedom is not explicitly treated in our dynamical model. Nonetheless, the dynamics depends through the Wigner rotational matrix on the quantum number M, which specifies the orientation of the impinging H$_2$O molecule. It should be noted that due to the symmetry of the 6D potential ($V(\varphi) = V(2\pi - \varphi)$), only cosine functions are needed when M equals 0. However, for $M > 0$ case, the exponential Fourier function needs to be expanded as both sine and cosine functions, resulting in two separate blocks in the vector-matrix multiplication and both contributing to the propagation.

The reaction probabilities were calculated using the time-independent version of Chebyshev real wave packet (CRWP) method (35), which has been recently applied to atom-triatom systems. Similar to the conventional time-dependent wave packet method, an initial wave packet associated with a particular ro-vibrational state of the reactant (D$_2$O) above the surface is launched and propagated using the Chebyshev three-term recursion formula. The total reaction probability is determined using a flux method on a dividing surface placed beyond the saddle point. Since only one OD bond is allowed to break in our model, all reaction probabilities have been multiplied with a factor of two to account for both reaction channels.

<u>S-IId.</u> <u>Corrections</u> <u>for</u> <u>Site</u> <u>and</u> <u>Lattice</u> <u>Effects</u>

Due to the absence of the *X* and *Y* coordinates, our 6D model neglects sites on the Ni(111) surface that have higher barriers than that along the MEP. In addition, effects of surface atom motion are also ignored in our model. Jackson and coworkers have extensively studied these effects for dissociative chemisorption of CH$_4$ on various metal surfaces (*14, 37, 65-66*), and their treatments within the sudden approximation have successfully reproduced the experimentally observed surface temperature dependence of dissociative sticking coefficients. Very recently, we have employed their models to incorporate site and lattice effects in our eight-dimensional quantum dynamical calculations on the CH$_4$ dissociation on Ni(111), and obtained excellent agreement with experimental data (*15*). Here, these well-tested models were used to correct the site and lattice effects in the dissociative chemisorption of D$_2$O on Ni(111).

Following Jackson and Nave (*14*), the barrier corrugation is approximately described as follows:

$$\Delta V(X,Y) = \frac{1}{2} M \left\{ \omega_x^2 [X - X_{TS}]^2 + \omega_y^2 [Y - Y_{TS}]^2 \right\}, \tag{7}$$

where X_{TS} and Y_{TS} are the lateral coordinates of the transition state, *M* is the mass for D$_2$O and ΔV is the difference between the barriers at (*X, Y*) and (X_{TS}, Y_{TS}). The vibrational frequencies for lateral motion at the transition state, ω_x and ω_y, are calculated on Ni(111) to be 150 and 78 cm^{-1}, respectively. A further assumption is made that reaction probabilities at different impact sites have the same energy dependence, but varying with the barrier height. As a result, the probability for a specific (*X, Y*) site is approximated by shifting the ΔV =0 probability (*14*):

$$\Theta(E_Z; X, Y) \approx \Theta_0[E_Z - \Delta V(X,Y); X_{TS}, Y_{TS}], \tag{8}$$

where Θ_0 is the reaction probability obtained by quantum wavepacket calculations on our PES, namely when (*X, Y*)= (X_{TS}, Y_{TS}), Θ is thus the probability at a different site (*X, Y*), and $\Delta V(X,Y)$ is the barrier shift. We then average over the results for many (*X, Y*) sites which cover the surface unit cell, sampling all possible impact sites on the surface. The consequence of the site-averaging is an increased effective barrier and shift of the probability curve towards a higher energy. This site-averaging model has been shown to work well for the dissociative chemisorption of H$_2$ on the Cu(111) surface (*67*) and that of CH$_4$ on the Ni(100)/Ni(111) surfaces (*14, 66*).

The so-called "electronic coupling" and "mechanical coupling", which represent respectively the change of the barrier height and barrier location when the surface atoms move, are taken into account subsequently. The former can be reasonably described by a potential term $-\beta Q$ (*14, 68*), where *Q* is the displacement of a surface Ni atom from the surface plane. The later can be described by a shift of barrier location along the surface normal, which equals αQ (*14, 37, 68*). It has been shown by Jackson and coworkers (*14, 37, 65*) that the electronic coupling can be reasonably approximated within a sudden approximation due to the large mass of the Ni atom, while the mechanical coupling can be treated using a surface mass model (*37, 69*). Several surface atoms were found to have notable β values with the largest β of 0.64 eV/Å and those with β values larger than 0.1 eV/Å were included to simulate the electronic coupling. On the other hand, mechanical coupling only involves the motion of the Ni atom directly under

D$_2$O, which only puckers up by 0.12 Å and leads to vertical location of the barrier shifts up by 0.089 Å, resulting in α =0.72. The overall lattice effects in the H$_2$O/Ni(111) system are smaller than those in CH$_4$/Ni(111) case, but similar to CH$_4$ dissociation on Pt(110)-(1×2) surface(*36*).

In actual calculations, we first model the mechanical coupling by substituting the collision coordinate *Z* with $Z' = Z - \alpha Q$ and the corresponding mass M in Eq. (6) with $\mu_T = M_s' M / (M_s' + M)$, where $M_s' = M_s / \alpha^2$ and M_s is the mass of the Ni atom. The reaction probability is then computed with the mass-modified Hamiltonian with *Q*=0. The resulting single-site reaction probability $\Theta_{\text{single-site}}^{Q=0}(E_{COM})$ is then averaged over all possible (*X*, *Y*) sites to yield the site-averaged reaction probability $\Theta_{\text{site-averaged}}^{Q=0}(E_{COM})$, using the method discussed above. The site averaging is followed by the correction of the electronic coupling, which is approximated by a Boltzmann sampling of *Q* using an *E*-shifting scheme, in which the probability for $Q \neq 0$ is obtained by a shift with an amount of barrier difference with *Q*=0 (namely $-\beta Q$). Finally, this probability $\Theta_{\text{site-averaged}}^{Q-\text{averaged}}(E_{COM})$ can be averaged over the lattice atom momentum *P* to include the mechanical coupling, providing the final temperature dependent initial sticking probability $S_0(E_Z, T)$ as function of normal incident energy (*E*$_Z$). In practice, the integral averaged over *P* can be converted to one over E_{COM} as (*37*),

$$S_0(E_Z, T) = \int dE_{COM} \sqrt{\frac{M_s'}{4\pi T \mu_T E_{COM}}} e^{-\frac{M_{s'}}{2k_B T}\left(\sqrt{\frac{2E_{com}}{\mu_T}} - \sqrt{\frac{2E_Z}{M}}\right)^2} \Theta_{\text{site-averaged}}^{Q-\text{averaged}}(E_{COM}). \qquad (9)$$

Here, *T* is the surface temperature and k_B is Boltzmann constant. The COM collision energy (E_{COM}) is related to the lattice atom momentum (*P*) as follows

$$E_{com} = \frac{1}{2}\mu_T \left(\sqrt{\frac{2E_Z}{M}} - \alpha \frac{P}{M_s}\right)^2, \qquad (10)$$

where the term in parenthesis is the relative D$_2$O-lattice atom collision velocity for a given incident energy *E*$_Z$ and lattice atom momentum *P*. We note in passing that the site and lattice effects are assumed to be the same for each vibrational state, which constituents an additional approximation.

S-IIe. Scaled Potential Energy Surface
With the original DFT PES, the calculated initial sticking coefficients were found to systematically overestimate the experimental values for both the laser-on and off conditions. This discrepancy was attributed to the underestimation of barrier height using the PW91 functional. Similar underestimation of barrier heights by the PW91 functional was noted before by Kroes and coworkers (*40-42*), who investigated the H$_2$ dissociation on Cu surfaces. To accurately reproduce experimental results, these authors proposed a specific reaction parameter (SRP) functional, consisting of the PW91 and RPBE functionals with a ratio about 1:1, which effectively increases the barrier height (*40-42*). We have tested the influence of different functionals on the barrier height for water dissociative chemisorption on Ni(111) and found that the PW91 and PBE functionals give very similar results but the RPBE functional yields a

higher barrier with respect to the adsorption site by 16.4 kJ/mol. On the other hand, the saddle points obtained with the three functionals are geometrically very similar. The transition state geometries are compared in the lower panel of Fig. S4.

To correct the overestimation of the PW91 PES, we elected to employ a simple scaling function. To this end, an exponential function in Z coordinate was used, and the scaled energy is expressed as,

$$V_{scaled} = V \times (1 + \exp(-\lambda Z)),\tag{11}$$

where λ is chosen to be 1.0 Å^{-1}. This correction increases the barrier height by about 9.7 kJ/mol which is just between the predictions of the PW91 and RPBE functionals. The scaling has a minimal impact on the geometries for saddle point and adsorption site. In particular, the coordinates of Z and r_2 at transition state on the raw potential (Z=1.899 Å, r_2= 1.586 Å) and the scaled potential (Z=1.905 Å, r_2= 1.595 Å) are almost the same.

S-IIf. Additional Results
A.   DFT calculations

The optimized structures for IS, FS, and TS on rigid Ni(111) obtained by the CI-NEB method with the PW91 functional are shown in Fig. S4. The barrier height and transition-state geometry converged well with respect to the number of layers, the number of k-points, the size of unit cell, and the kinetic energy cutoff, as shown in Table S1. The corresponding adsorption and activation energies also compare well with those reported in various earlier studies in Table S2. Consistent with previous studies (70-74), the H_2O molecule at IS is preferentially adsorbed with the oxygen at 2.38 Å above the top of a Ni atom and the molecule plane is almost parallel to the surface. On the other hand, the dissociated OH and H fragments are co-adsorbed at the nearest fcc sites, also in agreement with earlier observations. At TS, the dissociating OH bond is elongated to 1.54 Å with the other O-H bond approximately maintaining its equilibrium bond length (0.98 Å), while the oxygen is shifted somewhat from the top site. The adsorption and activation energies are in generally good agreement with earlier results. It is important to note that in all theoretical studies, the dissociating O-H bond is significantly elongated at the saddle point comparing to its equilibrium value. This "late" barrier suggests that the vibrational excitation in H_2O should lead large enhancement on the reactivity.

At the transition state, the displacements of surface atoms along the Z direction, their positions are labeled in Fig. S5 (lower panel) and corresponding β values are listed in Table S3.

B.   Potential energy surface

The overall root mean square error (RMSE) for the fit of the H_2O + Ni(111) PES is 5.1 kJ/mol, but significantly smaller (2.0 kJ/mol) for points below 145 kJ/mol. The overall RMSE for the fit for H_2O in gas phase is only 1.6 kJ/mol (1.1 kJ/mol for points below 145 kJ/mol). The 6D PES is displayed in Fig. 1, which shows a contour plot as a function of r_2 and Z, with other coordinates relaxed. The "late" barrier can be clearly seen in this figure. Stationary points of the fitted PES with the DFT calculations are further compared in Table S4, where geometries, energies and zero-point energies (ZPEs), and harmonic vibrational frequencies are listed. For the isolated H_2O, its geometry is close to experiment. Its harmonic vibrational frequencies for the symmetric stretching, bending, and antisymmetric stretching modes (3701,

1578, 3824 cm^{-1}) on the PES reproduce the DFT values quite well, which are also in reasonably good agreement with the experimental values (3832, 1648, 3942 cm^{-1}). These frequencies decrease slightly when H$_2$O is physisorbed on the top site, indicating its weak interaction with the metal surface, in accordance with earlier investigations. At the transition state, the high frequency mode corresponds to the stretch of the non-reactive OH, while the other OH stretching and bending frequencies are significantly lowered from those of isolated water, indicating mode softening as H$_2$O dissociates.

C.   Quantum Dynamics

To achieve numerical convergence, 90 sine DVR grid points were used in the interaction region of the translational coordinate Z, [2.0-6.2] bohr. 28 vibrational basis functions were used in the interaction region in r_2, [1.0-5.5] bohr. In the asymptotic region, 190 sine DVR grid points were used for $Z \in$ [6.2, 15.0] bohr, 6 vibrational basis functions in r_2 were used for the ground vibrational state (8 for stretching excited states). The non-reactive r_1 coordinate was discretized with 6 PODVR points (7 PODVR for stretching excited states). The numbers of grids in angular coordinates were $(j, J, K) = (26, 35, 26)$. We placed the initial wavepacket at Z=12.5 bohr (S_1) and the dividing surface for flux analysis at r_2=3.5 bohr (S_2), respectively. The damping potential is defined as an exponential function in Z and r_2 coordinates, $D(\zeta)) = \exp(-\gamma(\zeta - \zeta_d)^2 /(\zeta_{max} - \zeta_d)^2)$ ($\zeta = Z$ or r_2), starting from Z_d=13.0 bohr and r_{2d}=3.7 bohr, with γ=0.10. The spectral range of the discretized Hamiltonian for the ground vibrational state of D$_2$O ranges from -0.22 eV to 22.1 eV. About 8000 Chebyshev steps were needed to converge the reaction probabilities. These parameters have been extensively tested for convergence the probability up to translational of 1.25 eV. Only rotationless D$_2$O was considered.

The reaction probabilities obtained in the above dynamics calculations were used as the starting point for further corrections as described in Sec. S-IIc-d. In Fig. S5, the effects of various corrections are displayed for the reactivity of the ground vibrational state of D$_2$O. As expected, averaging over the impact sites in the unit cell decreases the reaction probability, due apparently to the increase of the effective barrier height. In addition, the "electronic coupling" increases the reactivity somewhat at very low translational energies. Nevertheless, this lattice effect is not as prominent as that in the dissociative chemisorption of CH$_4$ on Ni(111) surface (15, 66), due apparently to the smaller β values. Indeed, this is consistent with the observation of Jackson and co-workers in the CH$_4$ dissociation on the Pt(110)-(1×2) surface (36), where the overall effect coming from several small β values is also small. On the other hand, the "mechanical coupling", which is taken into account by averaging over P, lowers the overall reactivity, especially at high energies, in accord with "recoil effects" that present the energy transfer from impinging molecule to the lattice (14). Interestingly, the "mechanical coupling" seems to contribute more here than what has been observed in CH$_4$ dissociation (15). It is clear from the figure that these corrections are critical to achieve a good agreement with the experimental data shown in Fig. 3.

The dissociative sticking probabilities obtained for the ground and singly excited vibrational states are compared in Fig. S6. It can be seen that both translational and vibrational excitations enhance the reaction, and two stretching modes have the largest and comparable enhancements. In order to estimate the vibrational efficacies in a large energy range, the quantum dissociation probability for the ground vibrational state of D$_2$O was extended up to the translational energy of 2.0 eV, which ensures the convergence of sticking coefficients up to 1.7 eV after the surface effect corrections. This was achieved with an additional wave packet propagation with 320 grid points for the Z coordinate and an initial wave

packet with 1.6 eV of kinetic energy), The vibrational efficacies were then evaluated by the ratio of the translational energy difference at a given sticking coefficients of both ground and excited states and the vibrational energy gap. In particular, the logarithms of sticking coefficients were selected at -6, -5.5, -5, -4.5, -4, -3.5, -3, -2.5, -2. The calculated vibrational efficacies are listed in Table. S5. It is shown that all vibrational modes are more effective than the same amount of translational energy, leading to high vibrational efficacies. On the other hand, these vibrational efficacies depend on the energy (or sticking probability). The results obtained on the PW91 original potential are also shown for comparison, indeed, the slight increase of barrier height on the scaled potential brings the calculated dissociative sticking probabilities close to experimental data.

While consistent with Polanyi's rules (*26*) due to the late barrier, the large vibrational efficacies, particularly for the two stretching modes of D_2O, can be better rationalized by the recently proposed Sudden Vector Projection (SVP) model (*35, 44*). In the SVP model, the reaction is assumed to be sudden and the enhancement effect of a reactant mode is attributed to its coupling with the reaction coordinate, quantified by the alignment of the reactant normal mode vector with the reaction coordinate vector at the transition state: $0 \leq \vec{Q}_r \cdot \vec{Q}_{RC} \leq 1$. The SVP values for the antisymmetric and symmetric stretching modes of D_2O (0.65 and 0.67) are significantly larger than the translational mode (0.35), thus consistent with their remarkably large and comparable vibrational efficacies. The situation here is very different from that of the dissociative chemisorption of methane on Ni(111), where the SVP values for the two stretching vibrational modes and translation are quite similar (*75*), as shown in Fig. S7.

It should be noted that bending excitation also shows significant enhancement over the translation. This is consistent with findings in our previous dynamics calculations for the $H_2O/Cu(111)$ system (*17*), but is underestimated by the SVP model, which predicts a small overlap (0.09) between the bending mode and the reaction coordinate. The less reliable prediction of bending efficacies by the SVP model has been noted before (*35*). On the other hand, it is worthwhile to note that the significant decrease of the bending frequency at transition state (563 cm^{-1}) versus that of D_2O in gas phase (1148 cm^{-1}), resulting in a lower vibrationally adiabatic barrier for bending excited state. The large enhancement of bending excitation is therefore partially understandable within the vibrationally adiabatic theory (*76*).

Due to the large efficacies of various vibrational states, many low-lying vibrational states have appreciable contributions to the laser-off data measured with nozzle temperatures of 573, 673, and 773 K, respectively. In our simulations, several low-lying vibrational states of D_2O were considered and the theoretical laser-off data were obtained as a Boltzmann average of the sticking probabilities from these states. In the laser-on experiments, only a specific vibrational state was populated, the theoretical sticking probability was also state-specific. The comparison of experiments and theory is shown in Fig. 3 and the agreement is quite satisfactory, given the complexity of the system. The contributions of individual vibrational states to the laser-off data at 773 K are compared in Fig. S8. It is clear that the contribution of the ground vibrational state of D_2O is almost negligible at the experimental translational energies, and the laser-off reactivity is actually dominated by several excited vibrational states.

The situation here is reminiscent of what has been observed in $H+H_2O \rightarrow H_2+OH$ reaction in gas phase (*43*), which bares many similarities with the present reaction on surface. Both reactions have a "late" barrier and a high barrier height. It was found that thermal rate coefficients for the $H+H_2O$ abstraction reaction are dominated by contributions from the excited

H_2O stretching vibrational states and the ground vibrational state contribution for reactivity is about two orders of magnitude smaller than thermal ones (*43*). It is important to note the difference between this case and other experiments for CH_4 dissociation on Ni surfaces. In the latter case, the laser-off data were considered to be close to the sticking coefficient for the ground vibrational state of CH_4, based on the assumption that all excited states have the same unit vibrational efficacy (*3*). While this is roughly true for CH_4 dissociation on Ni(111) surfaces, it appears not the case for D_2O on Ni(111) as shown here. In other words, the experimental laser-off data reported here cannot be equated with the ground vibrational state results.
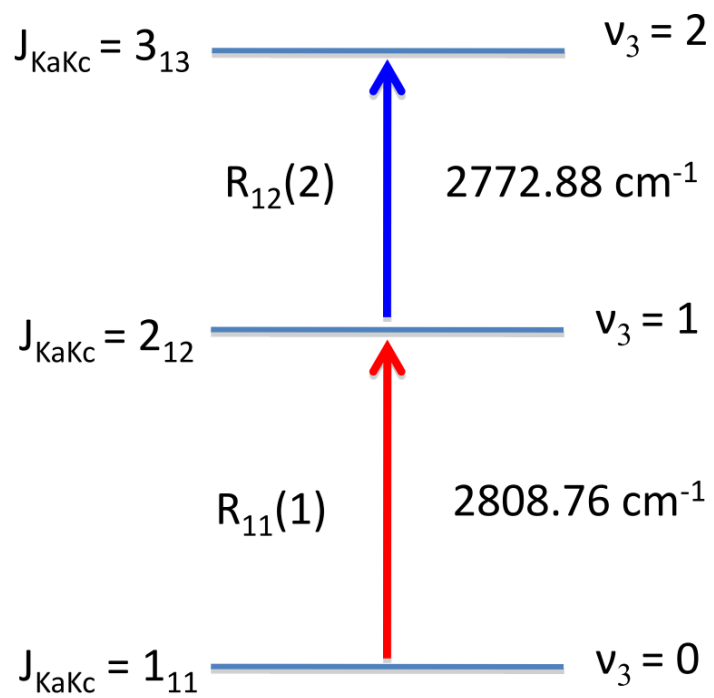
Fig. S1. Level diagram of the transitions used for D_2O excitation in the molecular beam.
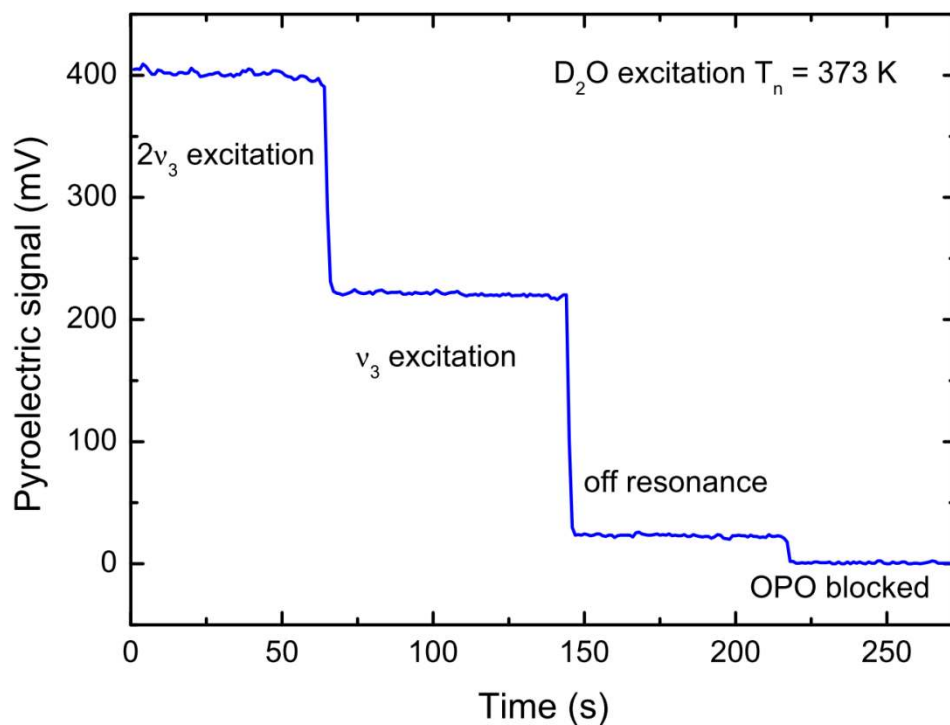
Fig. S2. The pyroelectric detector signal used to quantify the flux of vibrationally excited D_2O molecules in the molecular beam obtained by infrared pumping. The first 60s show the signal detected for double-resonance excitation of the $2\nu_3$, $J_{KaKc}=3_{13}$ state using both OPO-1 and OPO-2. At T=60 sec, OPO-2 is blocked to perform single photon excitation of the ν_3, $J_{KaKc}=2_{12}$ state by only OPO-1. At t=150 sec, both OPOs are passing through the molecular beam but are detuned from resonance to determine the background signal due to scattered IR light. Finally, at 215 sec both OPOs are blocked to record the baseline signal.
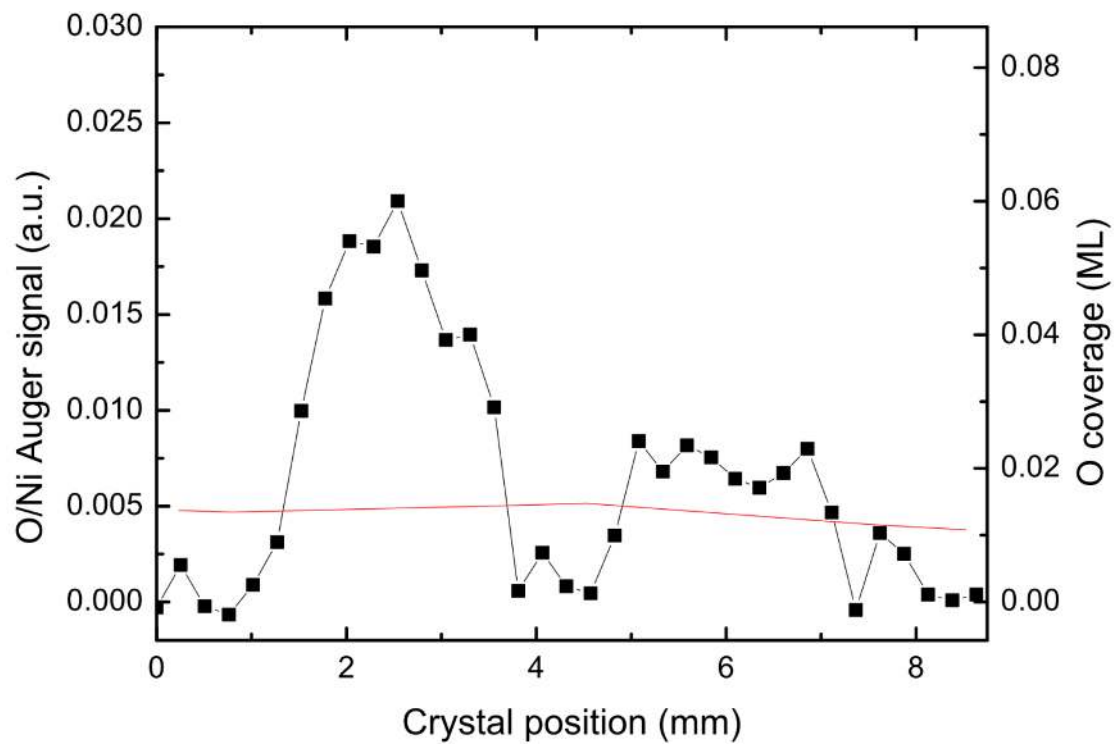
Fig. S3. An AES profile scan of two oxygen "footprints" formed on the Ni(111) surface at Ts=300 K by D_2O dissociation after subtraction of an adjustable baseline (shown in red) consisting of 6 points.
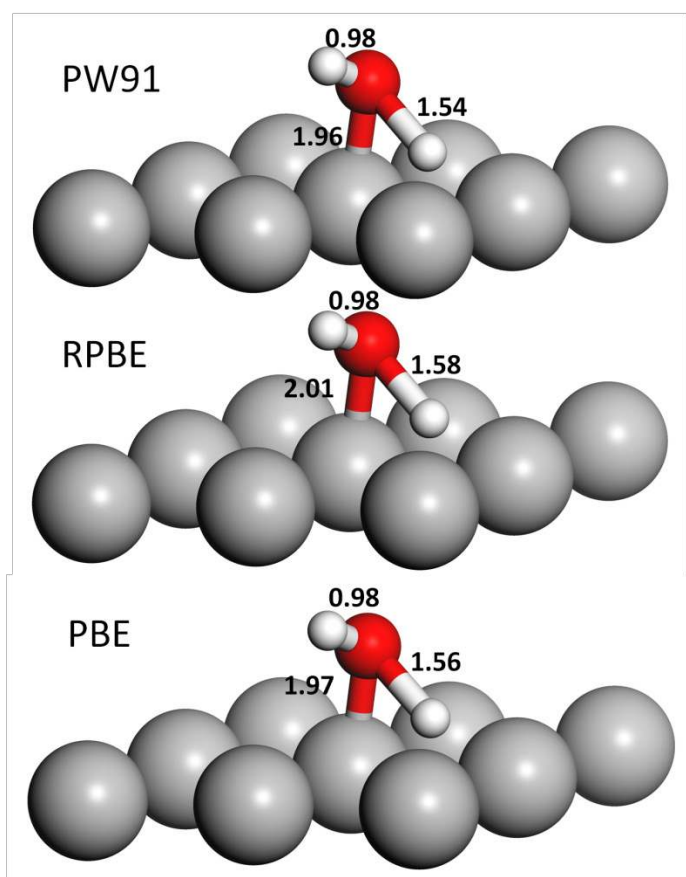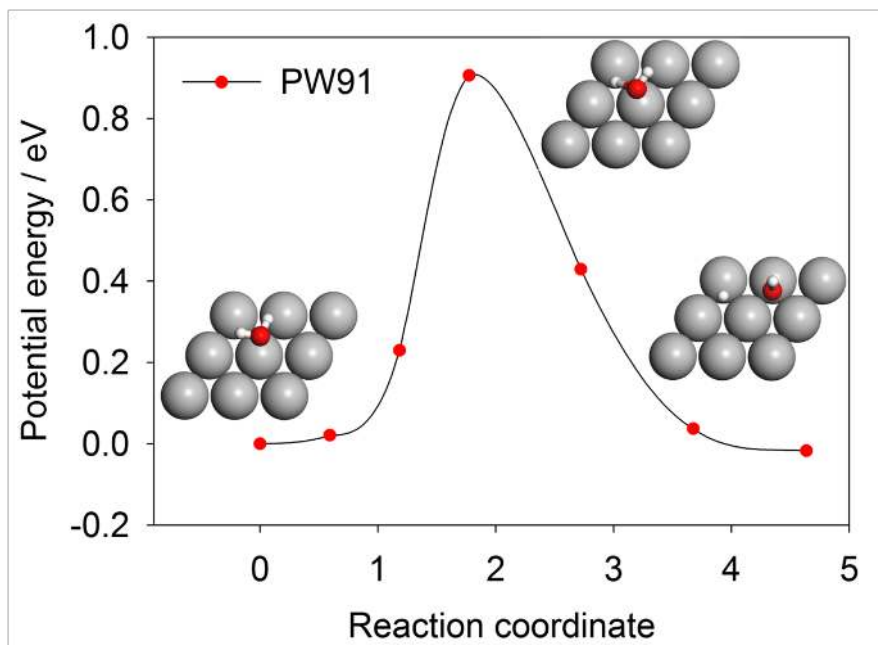
Fig. S4. The upper panel shows stationary points along the reaction path for the dissociative chemisorption of H_2O on Ni(111) obtained by the CI-NEB method using PW91 functional. The lower panel compares transition state geometries obtained from different functionals in terms of the lengths of two OH bonds and the distance of O-Ni.
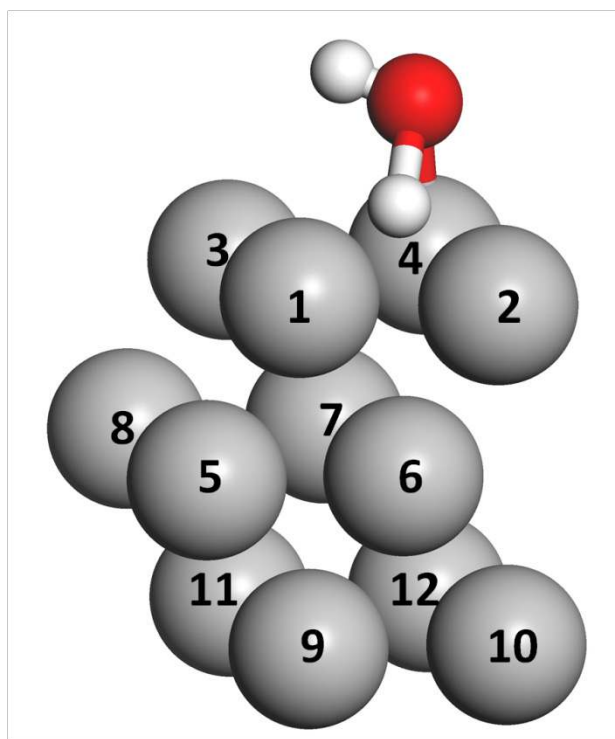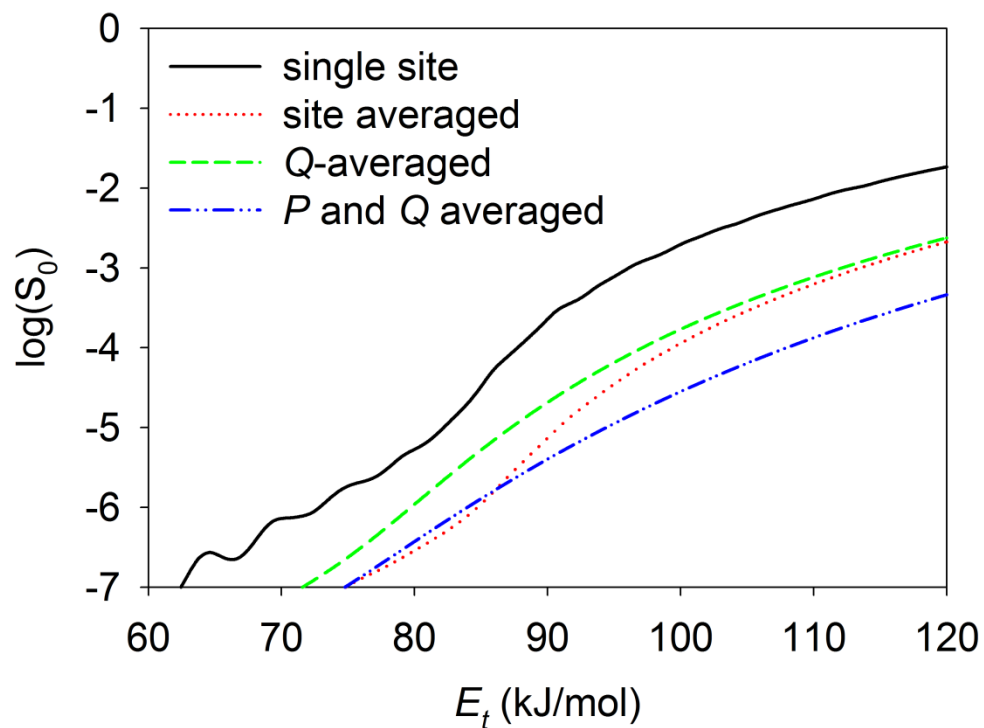
Fig. S5. The upper panel illustrates the effects of various corrections on the reaction probability for the ground vibrational state of D_2O on Ni(111). The lower panel defines the atoms in the slab model, in which the surface atoms in the top two layers were used for correction of lattice motions.
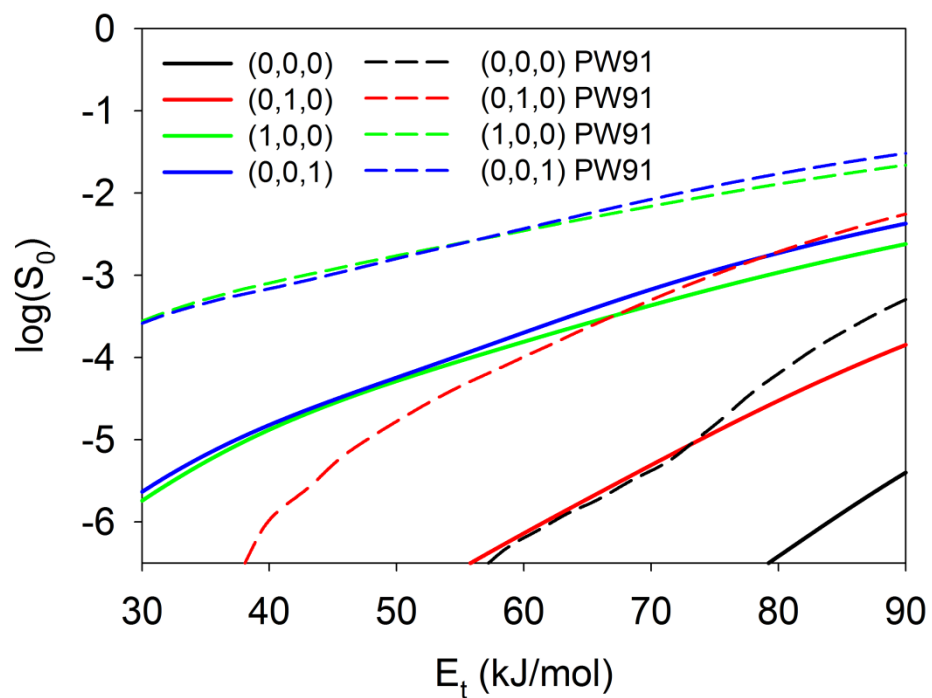
Fig. S6. Reaction probabilities for both the ground and excited vibrational states of D_2O as a function of the translational energy. Solid lines are obtained on the scaled potential, while dashed ones are on the PW91 original potential.
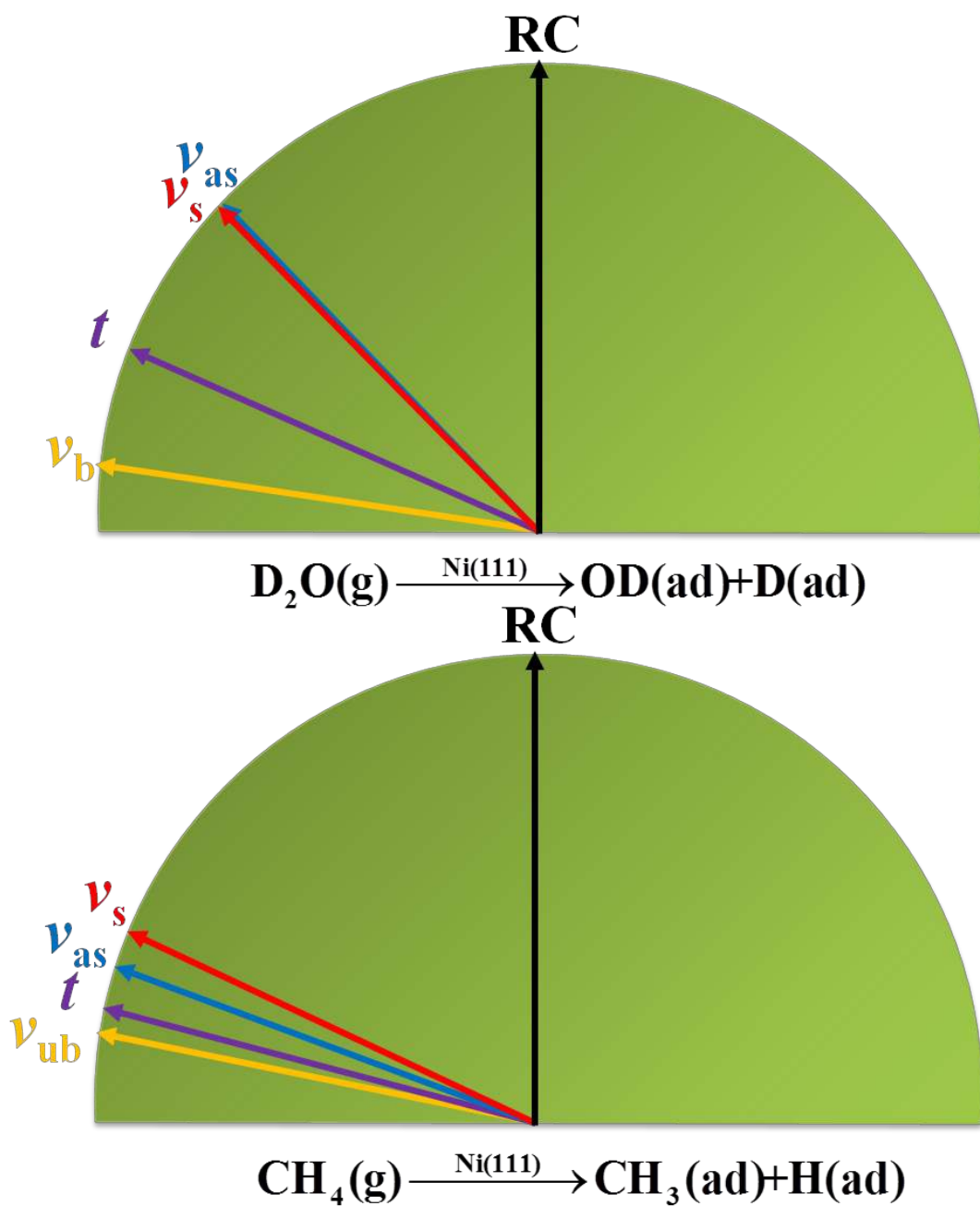
RC

v_{as}
v_s

t

v_b

$D_2O(g) \xrightarrow{\text{Ni(111)}} OD(ad)+D(ad)$

RC

v_s
v_{as}
t
v_{ub}

$CH_4(g) \xrightarrow{\text{Ni(111)}} CH_3(ad)+H(ad)$

Fig. S7. Alignments of various reactant modes with the reaction coordinate (RC) at the transition state for the dissociative chemisorption of D_2O and CH_4 on Ni(111).
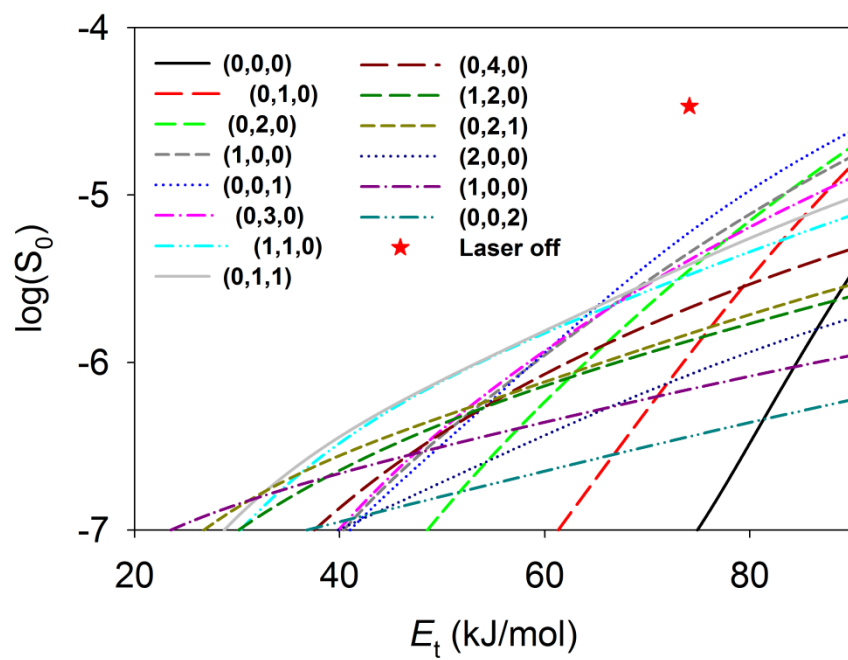
Fig. S8. Contributions of various vibrational states of D_2O to the initial sticking probability at 773 K.

Table S1. Convergence tests with respect to number of k points, size of unit cell, number of layers, kinetic energy cutoff of plane wave basis, as well as the relaxation of surface atoms. The kinetic energy cutoff is 400 eV except for the last three lines which were performed to check the convergence. The surface atoms were kept at their bulk positions unless stated elsewhere. The results from the work of Seenivasan and Tiwari (Ref. (*21*)) are included for comparison.

Functional	k points	Unit cell	Layers	E_{ad}(eV)	E_a(eV)	d_{OH} (Å)
CI-NEB calculations						
PBE[a]	8×8×1	2×2	4	0.17	0.795	1.48
PBE	3×3×1	2×2	4	0.21	0.63	1.569
PBE	5×5×1	2×2	4	0.19	0.65	1.555
PBE	8×8×1	2×2	4	0.19	0.67	1.553
PW91	3×3×1	2×2	3	0.23	0.67	1.544
PW91	5×5×1	2×2	3	0.25	0.65	1.556
PW91	8×8×1	2×2	3	0.24	0.65	1.546
PW91	3×3×1	2×2	4	0.24	0.60	1.562
PW91	5×5×1	2×2	4	0.23	0.61	1.549
PW91	8×8×1	2×2	4	0.23	0.63	1.539
PW91[c]	3×3×1	2×2	3	0.24	0.65	1.540
PW91[d]	3×3×1	2×2	3	0.22	0.70	1.551
PW91[d]	8×8×1	2×2	4	0.24	0.64	1.559
Single point calculations						
PW91[b]	3×3×1	3×3	3	/	0.67	/
PW91[b]	5×5×1	3×3	3	/	0.64	/
PW91[b]	3×3×1	2×2	5	/	0.68	/
PW91[b]	5×5×1	2×2	5	/	0.64	/
PW91/350 eV[e]	3×3×1	2×2	3	/	0.67	/
PW91/450 eV[e]	3×3×1	2×2	3	/	0.68	/
PW91/500 eV[e]	3×3×1	2×2	3	/	0.68	/

[a]: From the work of Seenivasan and Tiwari (Ref. (*21*)).

[b]: The energy for transition state is obtained from a single point calculation based on the geometry of PW91/(8×8×1)/(2×2)/(4 layers) level. E_a is then estimated by the energy difference of transition state and the energy of H_2O molecule plus the clean surface. It should be noted that these single point calculations are much more (18-34 times) expensive than those using the parameters in our work.

[c]: The top two layers were always relaxed during optimization.

[d]: The top two layers were optimized in a clean surface and then fixed during optimization.

[e]: The energy for transition state is obtained from a single point calculation based on the geometry of PW91/(3×3×1)/(2×2)/(3 layers) level. E_a is then estimated by the energy difference of transition state and the energy of H_2O molecule plus the clean surface. These calculations consider the convergence with respect to kinetic energy cutoff.

Table S2. Comparison of calculated adsorption and activation energies of H_2O dissociation on Ni(111) surface. The dissociating O-H bond length is also listed for comparison when available. (Energy is in eV (1 eV = 96.485 kJ/mol), without ZPE correction, bond length is in angstrom).

Computational details	E_{abs} [a]	E_a [a]	$E_a{'}$ [a]	d_{OH}	Ref.
Three layers, 1/4 ML, 400eV, 3×3×1 k points PW91 / PAW	-0.23	0.90	0.67	1.544	This work
Three layers, 1/6 ML, 340eV, 4×6×1 k points PBE /Troullier-Martines PP	/	0.74	/	1.881	(70)[b]
Three layers, 1/4 ML, 408eV, 15 k points PW91 / USPP	-0.25	0.89	0.64	/	(77)
Three layers, 1/9 ML, 400eV, 3×3×1 k points PBE / USPP	-0.29	0.96	0.67	1.56	(49)
Four layers, 1/4 ML, 476eV, 4×4×1 k points PW91 / USPP	-0.20	/	/	/	(78)
Four layers, 1/9 ML, 400eV, 3×3×1 k points PBE / PAW	-0.29	0.92	0.63	/	(79)
Three to five layers, 1/4 ML, 340eV, a Chadi–Cohen k point set RPBE / USPP	-0.01	0.94	0.93	/	(80)
Three layers, 1/4 ML, 816eV, 3×3×1 k points PBE / Troullier-Martins PP	-0.24	/	/	/	(81)
Four layers, 1/4 ML, 2720eV, 5×5×1 k points PBE / Troullier-Martins PP	-0.47	0.90	0.43	1.586	(82)
Three layers, 1/4 ML, 340eV, 6×6×1 k points RPBE / USPP	-0.02	0.92	0.90	/	(83)
Four layers, 1/4 ML, 400eV, 8×8×1 k points PBE / PAW	-0.17	0.96[c]	0.79	1.48	(21)

[a]The adsorption energy is defined as $E_{ads} = E_{mole+slab} - E_{mole} - E_{slab}$, where $E_{mole+slab}$, E_{mole}, and E_{slab} are the total energies of the optimized molecule plus surface system, the adsorbate in the gas phase, and the clean surface, respectively. The activation energy E_a here is relative to E_{ads} in order to compare with earlier DFT calculations, $E_a{'}$ is the barrier height relative to the gas phase.

[b]In Ref. (70), spin-polarization was not implemented. In all other studies, spin-polarized DFT was employed.

[c]This value is adapted from Ref. (21), which reported an activation energy of 0.795 eV relative to H_2O in gas phase.

Table. S3. Displacement in Z and electronic coupling parameters β_i for surface atoms in top two layers. The numbering scheme is shown in Fig. S5 and Ni-4 is the one just under the O atom at the transition state.

Numbering i	d_i (Å)	β_i (eV/Å)
1	0.01	0.01
2	-0.03	-0.28
3	0.005	-0.04
4	0.12	0.63
5	0.01	-0.14
6	0.005	-0.06
7	-0.005	0.06
8	-0.006	-0.05

Table S4. Comparison of the properties of stationary points on the scaled PES and those obtained by the plane wave DFT optimization. The bond lengths are in bohr (1 bohr = 0.5292 Å), bond angles in degree, harmonic frequencies in cm^{-1}, zero point energies and energies relative to the potential of H_2O+Ni(111) asymptote in eV (1 eV = 96.485 kJ/mol).

Species	Geometry[a]/Frequency/Energy	Method	
		DFT	PES
H$_2$O in asymptote	r_{OH}	1.837	1.837
	θ_{HOH}	104.7	104.6
	ω_1	1582	1578
	ω_2	3711	3701
	ω_3	3825	3824
	ZPE	0.57	0.57
Adsorption site	r_1	1.85	1.85
	r_2	1.88	1.88
	Z	4.53	4.55
	θ_1	107.5	107.1
	θ_2	91.5	90.5
	φ	90.5	90.8
	ω_1	152	118
	ω_2	303	378
	ω_3	446	554
	ω_4	1547	1581
	ω_5	3573	3572
	ω_6	3676	3694
	ZPE	0.60	0.61
	Energy	-0.23	-0.24
Transition state	r_1	1.85	1.85
	r_2	2.95	2.95

	Z	3.63	3.63
	θ_1	105.6	106.7
	θ_2	54.2	53.8
	φ	108.7	108.5
	ω_1	404	421
	ω_2	637	572
	ω_3	741	719
	ω_4	891	888
	ω_5	3638	3694
	ω_i	829i	737i
	ZPE	0.39	0.39
	Energy	0.67	0.67
	ZPE correct barrier height	0.50	0.50

[a]The geometries are compared in Jacobi coordinates in our six dimensional model. The Cartesian coordinates obtained from DFT optimization are converted within the reduced-dimensional model.

Table S5. Calculated vibrational frequencies and for D_2O (n_{ss}, n_b, n_{as}) and the corresponding vibrational efficacies.

Assignment (n_{ss}, n_b, n_{as})	Vibrational frequency (cm^{-1})	Vibrational efficacy [a]
(0,1,0)	1126	1.51~1.66
(0,2,0)	2231	1.54~1.70
(1,0,0)	2579	1.54~1.83
(0,0,1)	2697	1.65~1.78
(0,3,0)	3316	1.59~1.62
(1,1,0)	3700	1.51~1.77
(0,1,1)	3814	1.66~1.79
(0,4,0)	4371	1.49~1.58
(1,2,0)	4798	1.57~1.66
(0,2,1)	4912	1.64~1.73
(2,0,0)	5094	1.49~1.67
(1,0,1)	5205	1.51~1.79
(0,0,2)	5353	1.29~1.74

[a] Calculated vibrational efficacy depends on the translational energy. These values are estimated at the logarithms of sticking coefficients being -6, -5.5, -5, -4.5, -4.0, -3.5, -3.0, -2.5, -2.0, when these sticking coefficients are available for both the ground and excited states.

Table S6. Calculated sticking coefficients (S_0) and Boltzmann populations (P) for various vibrational states at the three experimental nozzle temperatures and corresponding incident energies.

(n_{ss},n_b,n_{as})	573K (58.3 kJ/mol)		673K (65.6 kJ/mol)		773K (74.1 kJ/mol)	
	P	$Log(S_0)$	P	$Log(S_0)$	P	$Log(S_0)$
(0,0,0)	0.938	-7.61	0.903	-7.54	0.863	-7.07
(0,1,0)	0.0555	-7.54	0.0813	-6.76	0.106	-5.95
(0,2,0)	3.46×10^{-3}	-6.93	7.65×10^{-3}	-6.16	0.0136	-5.45
(1,0,0)	1.44×10^{-3}	-6.73	3.64×10^{-3}	-5.99	7.10×10^{-3}	-5.34
(0,0,1)	1.07×10^{-3}	-6.76	2.83×10^{-3}	-5.94	5.70×10^{-3}	-5.22
(0,3,0)	2.27×10^{-4}	-6.90	7.53×10^{-4}	-6.08	1.80×10^{-4}	-5.39
(1,1,0)	8.67×10^{-5}	-6.88	3.32×10^{-4}	-6.11	8.82×10^{-4}	-5.48
(0,1,1)	6.49×10^{-5}	-6.90	2.59×10^{-4}	-6.09	7.12×10^{-4}	-5.41
(0,4,0)	1.61×10^{-5}	-7.32	7.90×10^{-5}	-6.41	2.52×10^{-4}	-5.67
(1,2,0)	5.49×10^{-6}	-7.49	3.17×10^{-5}	-6.58	1.14×10^{-4}	-5.87
(0,2,1)	4.13×10^{-6}	-7.50	2.48×10^{-5}	-6.57	9.24×10^{-5}	-5.83
(2,0,0)	2.62×10^{-6}	-7.88	1.68×10^{-5}	-6.88	6.58×10^{-5}	-6.07
(1,0,1)	1.98×10^{-6}	-7.81	1.33×10^{-5}	-6.88	5.36×10^{-5}	-6.16
(0,0,2)	1.36×10^{-6}	-8.14	9.66×10^{-6}	-7.19	4.06×10^{-5}	-6.44
Laser off		-5.97		-5.17		-4.48

References and Notes

1. P. A. Thiel, T. E. Madey, The interaction of water with solid surfaces: Fundamental aspects. *Surf. Sci. Rep.* **7**, 211–385 (1987). doi:10.1016/0167-5729(87)90001-X

2. M. A. Henderson, The interaction of water with solid surfaces: Fundamental aspects revisited. *Surf. Sci. Rep.* **46**, 5 (2002). doi:10.1016/S0167-5729(01)00020-6

3. L. B. F. Juurlink, D. R. Killelea, A. L. Utz, State-resolved probes of methane dissociation dynamics. *Prog. Surf. Sci.* **84**, 69–134 (2009). doi:10.1016/j.progsurf.2009.01.001

4. R. D. Beck, P. Maroni, D. C. Papageorgopoulos, T. T. Dang, M. P. Schmid, T. R. Rizzo, Vibrational mode-specific reaction of methane on a nickel surface. *Science* **302**, 98–100 (2003). doi:10.1126/science.1088996 Medline

5. P. Maroni, D. C. Papageorgopoulos, M. Sacchi, T. T. Dang, R. D. Beck, T. R. Rizzo, State-resolved gas-surface reactivity of methane in the symmetric C-H stretch vibration on Ni(100). *Phys. Rev. Lett.* **94**, 246104 (2005). doi:10.1103/PhysRevLett.94.246104

6. L. B. F. Juurlink, R. R. Smith, D. R. Killelea, A. L. Utz, Comparative study of C-H stretch and bend vibrations in methane activation on Ni(100) and Ni(111). *Phys. Rev. Lett.* **94**, 208303 (2005). doi:10.1103/PhysRevLett.94.208303 Medline

7. D. R. Killelea, V. L. Campbell, N. S. Shuman, A. L. Utz, Bond-selective control of a heterogeneously catalyzed reaction. *Science* **319**, 790–793 (2008). doi:10.1126/science.1152819 Medline

8. L. Chen, H. Ueta, R. Bisson, R. D. Beck, Vibrationally bond-selected chemisorption of methane isotopologues on Pt(111) studied by reflection absorption infrared spectroscopy. *Faraday Discuss.* **157**, 285–295, discussion 375–398 (2012). doi:10.1039/c2fd20007d Medline

9. B. L. Yoder, R. Bisson, R. D. Beck, Steric effects in the chemisorption of vibrationally excited methane on Ni(100). *Science* **329**, 553–556 (2010). doi:10.1126/science.1191751 Medline

10. B. L. Yoder, R. Bisson, P. Morten Hundt, R. D. Beck, Alignment dependent chemisorption of vibrationally excited $CH_4(v3)$ on Ni(100), Ni(110), and Ni(111). *J. Chem. Phys.* **135**, 224703 (2011). doi:10.1063/1.3665136 Medline

11. V. A. Ukraintsev, I. Harrison, A statistical model for activated dissociative adsorption: Application to methane dissociation on Pt(111). *J. Chem. Phys.* **101**, 1564 (1994). doi:10.1063/1.468476

12. A. Bukoski, D. Blumling, I. Harrison, Microcanonical unimolecular rate theory at surfaces. I. Dissociative chemisorption of methane on Pt(111). *J. Chem. Phys.* **118**, 843 (2003). doi:10.1063/1.1525803

13. S. Nave, B. Jackson, Vibrational mode-selective chemistry: Methane dissociation on Ni(100). *Phys. Rev. B* **81**, 233408 (2010). doi:10.1103/PhysRevB.81.233408

14. B. Jackson, S. Nave, The dissociative chemisorption of methane on Ni(100): Reaction path description of mode-selective chemistry. *J. Chem. Phys.* **135**, 114701 (2011). doi:10.1063/1.3634073 Medline

15. B. Jiang, R. Liu, J. Li, D. Xie, M. Yang, H. Guo, Mode selectivity in methane dissociative chemisorption on Ni(111). *Chem. Sci.* **4**, 3249 (2013). doi:10.1039/c3sc51040a

16. F. Nattino, H. Ueta, H. Chadwick, M. E. van Reijzen, R. D. Beck, B. Jackson, M. C. van Hemert, G.-J. Kroes, Ab initio molecular dynamics calculations versus quantum-state-resolved experiments on CHD_3 + Pt(111): New insights into a prototypical gas-surface reaction. *J. Phys. Chem. Lett.* **5**, 1294–1299 (2014). doi:10.1021/jz500233n

17. B. Jiang, X. Ren, D. Xie, H. Guo, Enhancing dissociative chemisorption of H_2O on Cu(111) via vibrational excitation. *Proc. Natl. Acad. Sci. U.S.A.* **109**, 10224–10227 (2012). doi:10.1073/pnas.1203895109 Medline

18. B. Jiang, D. Xie, H. Guo, Vibrationally mediated bond selective dissociative chemisorption of HOD on Cu(111). *Chem. Sci.* **4**, 503 (2013). doi:10.1039/c2sc21393a

19. A. Mondal, H. Seenivasan, A. K. Tiwari, Water dissociation on Cu(111): Effects of molecular orientation, rotation, and vibration on reactivity. *J. Chem. Phys.* **137**, 094708 (2012). doi:10.1063/1.4749246 Medline

20. B. Jiang, J. Li, D. Xie, H. Guo, Effects of reactant internal excitation and orientation on dissociative chemisorption of H_2O on Cu(111): Quasi-seven-dimensional quantum dynamics on a refined potential energy surface. *J. Chem. Phys.* **138**, 044704 (2013). doi:10.1063/1.4776770 Medline

21. H. Seenivasan, A. K. Tiwari, Water dissociation on Ni(100) and Ni(111): Effect of surface temperature on reactivity. *J. Chem. Phys.* **139**, 174707 (2013). doi:10.1063/1.4827641

22. A. Sinha, M. C. Hsiao, F. F. Crim, Bond-selected bimolecular chemistry: H+HOD(4vOH)→OD+H_2. *J. Chem. Phys.* **92**, 6333 (1990). doi:10.1063/1.458312

23. M. C. Hsiao, A. Sinha, F. F. Crim, Energy disposal in the vibrational-state- and bond-selected reaction of water with hydrogen atoms. *J. Phys. Chem.* **95**, 8263–8267 (1991). doi:10.1021/j100174a046

24. M. J. Bronikowski, W. R. Simpson, R. N. Zare, Effect of reagent vibration on the hydrogen atom + water-d reaction: An example of bond-specific chemistry. *J. Phys. Chem.* **97**, 2194–2203 (1993). doi:10.1021/j100112a021

25. A. Sinha, J. D. Thoemke, F. F. Crim, Controlling bimolecular reactions: Mode and bond selected reaction of water with translationally excited chlorine atoms. *J. Chem. Phys.* **96**, 372 (1992). doi:10.1063/1.462473

26. J. C. Polanyi, Some concepts in reaction dynamics. *Science* **236**, 680–690 (1987). doi:10.1126/science.236.4802.680 Medline

27. H. Chadwick, P. M. Hundt, M. E. van Reijzen, B. L. Yoder, R. D. Beck, Quantum state specific reactant preparation in a molecular beam by rapid adiabatic passage. *J. Chem. Phys.* **140**, 034321 (2014). doi:10.1063/1.4861054

28. M. P. Schmid, P. Maroni, R. D. Beck, T. R. Rizzo, Molecular-beam/surface-science apparatus for state-resolved chemisorption studies using pulsed-laser preparation. *Rev. Sci. Instrum.* **74**, 4110 (2003). doi:10.1063/1.1599064

29. P. M. Hundt, R. Bisson, R. D. Beck, The sticking probability of D_2O-water on ice: Isotope effects and the influence of vibrational excitation. *J. Chem. Phys.* **137**, 074701 (2012). doi:10.1063/1.4742914 Medline

30. Materials and methods are available as supplementary materials on *Science* Online.

31. J. P. Perdew, K. A. Jackson, M. R. Pederson, D. J. Singh, C. Fiolhais, Atoms, molecules, solids, and surfaces: Applications of the generalized gradient approximation for exchange and correlation. *Phys. Rev. B* **46**, 6671–6687 (1992). doi:10.1103/PhysRevB.46.6671

32. G. Kresse, J. Furthmuller, Efficient iterative schemes for ab initio total-energy calculations using a plane-wave basis set. *Phys. Rev. B* **54**, 11169–11186 (1996). doi:10.1103/PhysRevB.54.11169

33. G. Kresse, J. Furthmuller, Efficiency of ab-initio total energy calculations for metals and semiconductors using a plane-wave basis set. *Comput. Mater. Sci.* **6**, 15–50 (1996). doi:10.1016/0927-0256(96)00008-0

34. J. M. Bowman, G. Czakó, B. Fu, High-dimensional ab initio potential energy surfaces for reaction dynamics calculations. *Phys. Chem. Chem. Phys.* **13**, 8094–8111 (2011). doi:10.1039/c0cp02722g Medline

35. B. Jiang, H. Guo, Control of mode/bond selectivity and product energy disposal by the transition state: X + H_2O (X = H, F, $O(^3P)$, and Cl) reactions. *J. Am. Chem. Soc.* **135**, 15251–15256 (2013). doi:10.1021/ja408422y Medline

36. D. Han, S. Nave, B. Jackson, Dissociative chemisorption of methane on Pt(110)-(1×2): Effects of lattice motion on reactions at step edges. *J. Phys. Chem. A* **117**, 8651–8659 (2013). doi:10.1021/jp402987w Medline

37. A. K. Tiwari, S. Nave, B. Jackson, The temperature dependence of methane dissociation on Ni(111) and Pt(111): Mixed quantum-classical studies of the lattice response. *J. Chem. Phys.* **132**, 134702 (2010). doi:10.1063/1.3357415 Medline

38. A. C. Luntz, A simple model for associative desorption and dissociative chemisorption. *J. Chem. Phys.* **113**, 6901 (2000). doi:10.1063/1.1311280

39. B. Hammer, L. B. Hansen, J. K. Nørskov, Improved adsorption energetics within density-functional theory using revised Perdew-Burke-Ernzerhof functionals. *Phys. Rev. B* **59**, 7413–7421 (1999). doi:10.1103/PhysRevB.59.7413

40. G.-J. Kroes, Towards chemically accurate simulation of molecule-surface reactions. *Phys. Chem. Chem. Phys.* **14**, 14966–14981 (2012). doi:10.1039/c2cp42471a Medline

41. C. Díaz, E. Pijper, R. A. Olsen, H. F. Busnengo, D. J. Auerbach, G. J. Kroes, Chemically accurate simulation of a prototypical surface reaction: H_2 dissociation on Cu(111). *Science* **326**, 832–834 (2009). doi:10.1126/science.1178722 Medline

42. L. Sementa, M. Wijzenbroek, B. J. van Kolck, M. F. Somers, A. Al-Halabi, H. F. Busnengo, R. A. Olsen, G. J. Kroes, M. Rutkowski, C. Thewes, N. F. Kleimeier, H. Zacharias, Reactive scattering of H_2 from Cu(100): Comparison of dynamics calculations based on the specific reaction parameter approach to density functional theory with experiment. *J. Chem. Phys.* **138**, 044708 (2013). doi:10.1063/1.4776224 Medline

43. D. H. Zhang, M. A. Collins, S.-Y. Lee, First-principles theory for the H + H_2O, D_2O reactions. *Science* **290**, 961–963 (2000). doi:10.1126/science.290.5493.961 Medline

44. B. Jiang, H. Guo, Relative efficacy of vibrational vs. translational excitation in promoting atom-diatom reactivity: Rigorous examination of Polanyi's rules and proposition of sudden vector projection (SVP) model. *J. Chem. Phys.* **138**, 234104 (2013). doi:10.1063/1.4810007 Medline

45. G.-J. Kroes, Frontiers in surface scattering simulations. *Science* **321**, 794–797 (2008). [doi:10.1126/science.1157717](#) [Medline](#)

46. D. R. Killelea, A. L. Utz, On the origin of mode- and bond-selectivity in vibrationally mediated reactions on surfaces. *Phys. Chem. Chem. Phys.* **15**, 20545–20554 (2013). [doi:10.1039/c3cp53765j](#) [Medline](#)

47. W. Demptröder, *Laser Spectroscopy: Experimental Techniques* (Springer, Berlin, ed. 4, 2008), vol. 2.

48. K. Christmann, R. J. Behm, G. Ertl, M. A. Vanhove, W. H. Weinberg, Chemisorption geometry of hydrogen on Ni(111): Order and disorder. *J. Chem. Phys.* **70**, 4168 (1979). [doi:10.1063/1.438041](#)

49. A. A. Phatak, W. N. Delgass, F. H. Ribeiro, W. F. Schneider, Density functional theory comparison of water dissociation steps on Cu, Au, Ni, Pd, and Pt. *J. Phys. Chem. C* **113**, 7269–7276 (2009). [doi:10.1021/jp810216b](#)

50. M. E. Gallagher, S. Haq, A. Omer, A. Hodgson, Water monolayer and multilayer adsorption on Ni(111). *Surf. Sci.* **601**, 268–273 (2007). [doi:10.1016/j.susc.2006.09.034](#)

51. P. E. Blöchl, Projector augmented-wave method. *Phys. Rev. B* **50**, 17953–17979 (1994). [doi:10.1103/PhysRevB.50.17953](#)

52. G. Kresse, D. Joubert, From ultrasoft pseudopotentials to the projector augmented-wave method. *Phys. Rev. B* **59**, 1758–1775 (1999). [doi:10.1103/PhysRevB.59.1758](#)

53. H. J. Monkhorst, J. D. Pack, Special points for Brillouin-zone integrations. *Phys. Rev. B* **13**, 5188–5192 (1976). [doi:10.1103/PhysRevB.13.5188](#)

54. J. P. Perdew, K. Burke, M. Ernzerhof, Generalized gradient approximation made simple. *Phys. Rev. Lett.* **77**, 3865–3868 (1996). [doi:10.1103/PhysRevLett.77.3865](#) [Medline](#)

55. J. P. Perdew, Y. Wang, Accurate and simple analytic representation of the electron-gas correlation energy. *Phys. Rev. B* **45**, 13244–13249 (1992). [doi:10.1103/PhysRevB.45.13244](#)

56. D. R. Lide, *CRC Handbook of Chemistry and Physics* (CRC Press, Boca Raton, FL, Internet Version 2005, 2005).

57. H. Jónsson, G. Mills, K. W. Jacobsen, in *Classical and Quantum Dynamics in Condensed Phase Simulations,* B. J. Berne, G. Ciccotti, D. F. Coker, Eds. (World Scientific, Singapore, 1998), 385–404.

58. G. Henkelman, B. P. Uberuaga, H. Jónsson, A climbing image nudged elastic band method for finding saddle points and minimum energy paths. *J. Chem. Phys.* **113**, 9901 (2000). [doi:10.1063/1.1329672](#)

59. G. P. Krishnamohan, R. A. Olsen, G.-J. Kroes, F. Gatti, S. Woittequand, Quantum dynamics of dissociative chemisorption of CH_4 on Ni(111): Influence of the bending vibration. *J. Chem. Phys.* **133**, 144308 (2010). [doi:10.1063/1.3491031](#) [Medline](#)

60. J. C. Light, T. Carrington Jr., Discrete-variable representations and their utilization. *Adv. Chem. Phys.* **114**, 263–310 (2000). [doi:10.1002/9780470141731.ch4](#)

61. D. T. Colbert, W. H. Miller, A novel discrete variable representation for quantum mechanical reactive scattering via the S-matrix Kohn method. *J. Chem. Phys.* **96**, 1982 (1992). doi:10.1063/1.462100

62. J. Echave, D. C. Clary, Potential optimized discrete variable representation. *Chem. Phys. Lett.* **190**, 225–230 (1992). doi:10.1016/0009-2614(92)85330-D

63. H. Wei, T. Carrington Jr., The discrete variable representation of a triatomic Hamiltonian in bond length–bond angle coordinates. *J. Chem. Phys.* **97**, 3029 (1992). doi:10.1063/1.463044

64. R. N. Zare, *Angular Momentum* (Wiley, New York, 1988).

65. A. K. Tiwari, S. Nave, B. Jackson, Methane dissociation on Ni(111): A new understanding of the lattice effect. *Phys. Rev. Lett.* **103**, 253201 (2009). doi:10.1103/PhysRevLett.103.253201 Medline

66. B. Jackson, S. Nave, The dissociative chemisorption of methane on Ni(111): The effects of molecular vibration and lattice motion. *J. Chem. Phys.* **138**, 174705 (2013). doi:10.1063/1.4802008 Medline

67. J. Dai, J. C. Light, Six dimensional quantum dynamics study for dissociative adsorption of H_2 on Cu(111) surface. *J. Chem. Phys.* **107**, 1676 (1997). doi:10.1063/1.474520

68. S. Nave, B. Jackson, Methane dissociation on Ni(111) and Pt(111): Energetic and dynamical studies. *J. Chem. Phys.* **130**, 054701 (2009). doi:10.1063/1.3065800 Medline

69. A. C. Luntz, J. Harris, CH_4 dissociation on metals: A quantum dynamics model. *Surf. Sci.* **258**, 397–426 (1991). doi:10.1016/0039-6028(91)90934-K

70. G.-C. Wang, S.-X. Tao, X.-H. Bu, A systematic theoretical study of water dissociation on clean and oxygen-preadsorbed transition metals. *J. Catal.* **244**, 10–16 (2006). doi:10.1016/j.jcat.2006.07.034

71. A. A. Gokhale, J. A. Dumesic, M. Mavrikakis, On the mechanism of low-temperature water gas shift reaction on copper. *J. Am. Chem. Soc.* **130**, 1402–1414 (2008). doi:10.1021/ja0768237 Medline

72. Q.-L. Tang, Z.-X. Chen, X. He, A theoretical study of the water gas shift reaction mechanism on Cu(111) model system. *Surf. Sci.* **603**, 2138–2144 (2009). doi:10.1016/j.susc.2009.04.011

73. X.-K. Gu, W.-X. Li, First-principles study on the origin of the different selectivities for methanol steam reforming on Cu(111) and Pd(111). *J. Phys. Chem. C* **114**, 21539–21547 (2010). doi:10.1021/jp107678d

74. J. L. C. Fajín, F. Illas, J. R. B. Gomes, Effect of the exchange-correlation potential and of surface relaxation on the description of the H_2O dissociation on Cu(111). *J. Chem. Phys.* **130**, 224702 (2009). doi:10.1063/1.3149851 Medline

75. B. Jiang, H. Guo, Mode and bond selectivities in methane dissociative chemisorption: Quasi-classical trajectory studies on twelve-dimensional potential energy surface. *J. Phys. Chem. C* **117**, 16127–16135 (2013). doi:10.1021/jp405720c

76. W. H. Miller, N. C. Handy, J. E. Adams, Reaction path Hamiltonian for polyatomic molecules. *J. Chem. Phys.* **72**, 99 (1980). doi:10.1063/1.438959

77. M. Pozzo, G. Carlini, R. Rosei, D. Alfè, Comparative study of water dissociation on Rh(111) and Ni(111) studied with first principles calculations. *J. Chem. Phys.* **126**, 164706 (2007). doi:10.1063/1.2717172 Medline

78. J. Li, S. Zhu, Y. Li, E. E. Oguzie, F. Wang, Electronic structure of monomeric water adsorption on Ni111: Beyond the general model. *J. Phys. Chem. C* **112**, 8301–8303 (2008). doi:10.1021/jp712070g

79. Y. A. Zhu, D. Chen, X. G. Zhou, W. K. Yuan, DFT studies of dry reforming of methane on Ni catalyst. *Catal. Today* **148**, 260–267 (2009). doi:10.1016/j.cattod.2009.08.022

80. H. S. Bengaard *et al*., Steam reforming and graphite formation on Ni catalysts. *J. Catal.* **209**, 365–384 (2002). doi:10.1006/jcat.2002.3579

81. D. Sebastiani, L. Delle Site, Adsorption of water molecules on flat and stepped nickel surfaces from first principles. *J. Chem. Theory Comput.* **1**, 78–82 (2005). doi:10.1021/ct049955o

82. R. C. Catapan, A. A. M. Oliveira, Y. Chen, D. G. Vlachos, DFT study of the water–gas shift reaction and coke formation on Ni(111) and Ni(211) surfaces. *J. Phys. Chem. C* **116**, 20281–20291 (2012). doi:10.1021/jp302488f

83. D. W. Blaylock, T. Ogura, W. H. Green, G. J. O. Beran, Computational investigation of thermochemistry and kinetics of steam methane reforming on Ni(111) under realistic conditions. *J. Phys. Chem. C* **113**, 4898–4908 (2009). doi:10.1021/jp806527q